

Free and smooth boundaries in 2-D finite-difference schemes for transient elastic waves

B. Lombard¹, J. Piraux¹, C. Gélis², J. Virieux²

¹ CNRS, Laboratoire de Mécanique et d'Acoustique, Marseille, France

² CNRS, Géosciences Azur, Sophia-Antipolis, France.

Received 200?; in original form 200?

SUMMARY

A method is proposed for accurately describing arbitrary-shaped free boundaries in finite-difference schemes for elastodynamics, in a time-domain velocity-stress framework. The basic idea is as follows: fictitious values of the solution are built in vacuum, and injected into the numerical integration scheme near boundaries. The most original feature of this method is the way in which these fictitious values are calculated. They are based on boundary conditions and compatibility conditions satisfied by the successive spatial derivatives of the solution, up to a given order that depends on the spatial accuracy of the integration scheme adopted. Since the work is mostly done during the preprocessing step, the extra computational cost is negligible. Stress-free conditions can be designed at any arbitrary order without any numerical instability, as numerically checked. Using 10 grid nodes per minimal S-wavelength with a propagation distance of 50 wavelengths yields highly accurate results. With 5 grid nodes per minimal S-wavelength, the solution is less accurate but still acceptable. A subcell resolution of the boundary inside the Cartesian meshing is obtained, and the spurious diffractions induced by staircase descriptions of boundaries are avoided. Contrary to what occurs with the vacuum method, the quality of the numerical solution obtained with this method is almost independent of the angle between the free boundary and the Cartesian meshing.

Key words: Free surface, Seismic modeling, Velocity-stress formulation, Numerical methods, Finite-difference methods, ADER schemes, Boundary conditions, Compatibility conditions.

1 INTRODUCTION

Various approaches have been proposed for simulating the propagation of elastic waves with free boundaries. The first approach is based on variational methods, as done in finite elements (Day, 1977), spectral finite elements (Komatitsch & Vilotte, 1998) and discontinuous Galerkin (Ben Jemaa et al., 2007). These methods provide a fine geometrical description of boundaries by adapting the mesh to the boundaries. Boundary conditions are accounted for weakly by the underlying variational formulation. However, a grid-generating tool is required, and small time steps may result from the smallest geometrical elements and from the stability condition. The SAT methods based on energy estimates (Carpenter et al., 1994) avoid these limitations by introducing Cartesian grids and give time-stable high-order schemes with interfaces. However and up to our knowledge, these methods have not been applied so far to elastodynamics with free boundaries.

The second approach used in this context is based on the strong form of elastodynamics, as done in finite differences and spectral methods (Tessmer & Kosloff, 1994). In seismology, finite differences are usually implemented on staggered Cartesian grids, either with completely staggered stencils (CSS) or with the recently

developed partially staggered stencils (PSS). With CSS, the velocity and stress components are distributed between different node positions (Virieux, 1986). With PSS, all the velocity components are computed at a single node, as are the stress components, although the latter are shifted by half a node in two separate grids. Second-order (Saenger et al., 2000; Saenger & Bohlen, 2004) and fourth-order (Bohlen & Saenger, 2003; Cruz-Atienza & Virieux, 2004) spatially-accurate PSS have been developed; for further discussion, we denote them PSS-2 and PSS-4, respectively. Unlike variational methods, finite differences require special care to incorporate the free boundary conditions strongly. There exist two main strategies for this purpose:

(i) First, the boundaries can be taken into account implicitly by adjusting the physical parameters locally (Kelly et al., 1976; Virieux, 1986; Muir et al., 1992). The best-known implicit approach is the so-called *vacuum method* (Zahradník, 1995; Graves, 1996; Moczo et al., 2002; Gélis et al., 2005). For instance, the vacuum method applied to PSS involves setting the elastic parameters in the vacuum to zero, and using a small density value in the first velocity node in the vacuum to avoid a division by zero. However, this easy-to-implement method gives at best second-order spatial accu-

racy. In addition, a systematic numerical study has shown that the accuracy of the solution decreases dramatically when the angle between the boundary and the meshing increases (Bohlen & Saenger, 2006). Lastly, applying the vacuum method sometimes gives rise to instabilities: see for instance PSS-4 (Bohlen & Saenger, 2003).

(ii) A second idea is to explicitly change the scheme near the boundaries (Kelly et al., 1976). The best-known explicit approach is the so-called *image method*, which was developed for dealing with flat boundaries to fourth-order accuracy (Levander, 1988) and then extended to variable topographies (Jih et al., 1988; Robertsson, 1996; Zhang & Chen, 2006). However image methods require a fine grid to reduce the spurious diffractions up to an acceptable level. To avoid this spatial oversampling, various techniques have been proposed, such as grid refinement in the vicinity of the boundary (Rodrigues, 1995) or adjusted finite-difference approximations: see (Moczo et al., 2007) for a review on these subjects.

The aim of this paper is to present a finite-difference approach accounting for free boundaries without introducing the aforementioned drawbacks of the vacuum and image methods. The requirements are as follows: smooth arbitrary-shaped boundaries must be treated as simply as straight boundaries; the accuracy of the method must not depend on the position of the boundary relative to the meshing; and lastly, the computations must be stable even with very long integration times. We establish that these requirements can be met by applying an explicit approach involving fictitious values of the solution in the vacuum. In previous studies, interface problems in the context of elastodynamics were investigated in a similar way (Piroux & Lombard, 2001; Lombard & Piroux, 2004, 2006). The fictitious values are high-order Taylor expansions of the boundary values of the solution. Estimating these boundary values involves some mathematical background, in order to compute the high-order boundary conditions; to determine a minimal set of independent boundary values; lastly, to perform a least-square numerical estimation of this minimal set. To help the reader, subroutines in FORTRAN are proposed freely at the web page <http://w3lma.cnrs-mrs.fr/~MI/Software/>. These subroutines enable a straightforward implementation of the algorithms detailed in the present paper.

The disadvantage here is that the above requirements cannot be fully satisfied if staggered-grid schemes are used. Single-grid finite-difference schemes are therefore chosen, where all the unknowns are computed at the same grid nodes. Our numerical experiments are based on the high-order ADER schemes which are widely used in aeroacoustics (Schwartzkopff et al., 2005). Although these schemes are not yet widely used in the field of seismology (Dumbser & Käser, 2006), they have also great qualities because of their accuracy and their stability properties: using 10 grid nodes per minimal S-wavelength with a propagation distance of 50 wavelengths gives highly accurate results. Moreover, on Cartesian grids, these methods do not require much more computational memory than staggered-grid schemes.

This paper is organized as follows. Section 2 deals with the continuous problem: the high-order boundary conditions and compatibility conditions are stated. These conditions are useful for handling the discrete problem presented in section 3, where the focus is on obtaining fictitious values of the solution in the vacuum. In section 4, numerical experiments confirm the efficiency of this method in the case of various topographies. In section 5, conclusions are drawn and some prospects suggested.

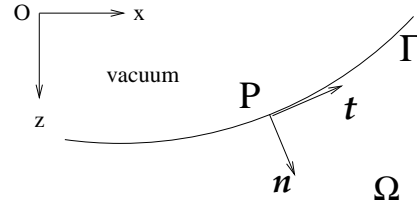


Figure 1. Boundary Γ between a solid Ω and vacuum.

2 THE CONTINUOUS PROBLEM

2.1 Framework

Let us consider a solid Ω separated from the vacuum by a boundary Γ (Figure 1). The configuration is in-plane and two-dimensional, with a horizontal axis x and a vertical axis z pointing respectively rightward and downward. The boundary Γ is described by a parametric expression $(x(\tau), z(\tau))$ where the parameter τ describes the sampling of the boundary. The tangential vector and the normal vector are $\mathbf{t} = {}^T(x'(\tau), z'(\tau))$ and $\mathbf{n} = {}^T(-z'(\tau), x'(\tau))$, respectively, with $x'(\tau) = \frac{dx}{d\tau}(\tau)$, $z'(\tau) = \frac{dz}{d\tau}(\tau)$, and T refers to the transposed vector. We assume the spatial derivatives at any point of the boundary to be available, as specified below.

The solid Ω is assumed to be linearly elastic, isotropic, and to have the following constant physical parameters: the density ρ and the Lamé coefficients λ, μ . The P- and S-wave velocities are $c_p = \sqrt{(\lambda + 2\mu)/\rho}$ and $c_s = \sqrt{\mu/\rho}$. A velocity-stress formulation is adopted, hence the unknowns are the horizontal and vertical components of the elastic velocity $\mathbf{v} = {}^T(v_x, v_z)$, and the independent components of the elastic stress tensor $\boldsymbol{\sigma} = {}^T(\sigma_{xx}, \sigma_{xz}, \sigma_{zz})$. Setting

$$\mathbf{A} = \begin{pmatrix} 0 & 0 & 1/\rho & 0 & 0 \\ 0 & 0 & 0 & 1/\rho & 0 \\ \lambda + 2\mu & 0 & 0 & 0 & 0 \\ 0 & \mu & 0 & 0 & 0 \\ \lambda & 0 & 0 & 0 & 0 \end{pmatrix},$$

$$\mathbf{B} = \begin{pmatrix} 0 & 0 & 0 & 1/\rho & 0 \\ 0 & 0 & 0 & 0 & 1/\rho \\ 0 & \lambda & 0 & 0 & 0 \\ \mu & 0 & 0 & 0 & 0 \\ 0 & \lambda + 2\mu & 0 & 0 & 0 \end{pmatrix},$$

the solution $\mathbf{U} = {}^T(v_x, v_z, \sigma_{xx}, \sigma_{xz}, \sigma_{zz})$ satisfies the first-order hyperbolic system (Virieux, 1986)

$$\frac{\partial}{\partial t} \mathbf{U} = \mathbf{A} \frac{\partial}{\partial x} \mathbf{U} + \mathbf{B} \frac{\partial}{\partial z} \mathbf{U}. \quad (1)$$

2.2 High-order boundary conditions

At any point $P(\tau)$ on the free surface Γ (Figure 1), the stress tensor satisfies the homogeneous Dirichlet conditions $\boldsymbol{\sigma} \cdot \mathbf{n} = \mathbf{0}$. These zero-th order boundary conditions are written compactly

$$\mathbf{L}^0(\tau) \mathbf{U}^0(x(\tau), z(\tau), t) = \mathbf{0}, \quad (2)$$

where \mathbf{U}^0 is the limit value of \mathbf{U} at P and \mathbf{L}^0 is the matrix

$$\mathbf{L}^0(\tau) = \begin{pmatrix} 0 & 0 & -z'(\tau) & x'(\tau) & 0 \\ 0 & 0 & 0 & -z'(\tau) & x'(\tau) \end{pmatrix}.$$

From now on, the dependence on τ is generally omitted. To determine the boundary conditions satisfied by the first-order spatial

derivatives of \mathbf{U} , two tasks are performed. First, the zeroth-order boundary conditions (2) are differentiated in terms of t . The time derivative is replaced by spatial derivatives using the conservation laws (1), which gives

$$\mathbf{L}^0 \left(\mathbf{A} \frac{\partial}{\partial x} \mathbf{U}^0 + \mathbf{B} \frac{\partial}{\partial z} \mathbf{U}^0 \right) = \mathbf{0}. \quad (3)$$

Secondly, the zeroth-order boundary conditions (2) are differentiated in terms of the parameter τ describing Γ . The chain-rule gives

$$\left(\frac{d}{d\tau} \mathbf{L}^0 \right) \mathbf{U}^0 + \mathbf{L}^0 \left(x' \frac{\partial}{\partial x} \mathbf{U}^0 + z' \frac{\partial}{\partial z} \mathbf{U}^0 \right) = \mathbf{0}. \quad (4)$$

Since the matrix $d\mathbf{L}^0/d\tau$ in (4) involves x'' and z'' , it accounts for the curvature of Γ at P . Setting the block matrix

$$\mathbf{L}^1 = \begin{pmatrix} \mathbf{L}^0 & \mathbf{0} & \mathbf{0} \\ \mathbf{0} & \mathbf{L}^0 \mathbf{A} & \mathbf{L}^0 \mathbf{B} \\ \frac{d}{d\tau} \mathbf{L}^0 & x' \mathbf{L}^0 & z' \mathbf{L}^0 \end{pmatrix},$$

equations (2), (3) and (4) give the boundary conditions up to the first-order

$$\mathbf{L}^1 \mathbf{U}^1 = \mathbf{0},$$

with

$$\mathbf{U}^1 = \lim_{M \in \Omega \rightarrow P} {}^T \left({}^T \mathbf{U}, \frac{\partial}{\partial x} {}^T \mathbf{U}, \frac{\partial}{\partial z} {}^T \mathbf{U} \right).$$

Let $k \geq 1$ be an integer whose value will be discussed in section 3. To get the boundary conditions up to the k -th order, one deduces from (2)

$$\frac{\partial^k}{\partial \tau^{k-\alpha} \partial t^\alpha} \mathbf{L}^0 \mathbf{U}^0 = \mathbf{0}, \quad \alpha = 0, \dots, k. \quad (5)$$

The τ -derivatives are replaced by spatial derivatives by applying $(k-\alpha)$ -times the chain rule. The t -derivatives are replaced by spatial derivatives by injecting α -times the conservation laws (1). The boundary conditions so-obtained up to the k -th order can be written compactly

$$\mathbf{L}^k \mathbf{U}^k = \mathbf{0}, \quad (6)$$

with

$$\mathbf{U}^k = \lim_{M \in \Omega \rightarrow P} {}^T \left({}^T \mathbf{U}, \dots, \frac{\partial^\alpha}{\partial x^{\alpha-\beta} \partial z^\beta} {}^T \mathbf{U}, \dots, \frac{\partial^k}{\partial z^k} {}^T \mathbf{U} \right), \quad (7)$$

where $\alpha = 0, \dots, k$ and $\beta = 0, \dots, \alpha$. The vector \mathbf{U}^k has $n_v = 5(k+1)(k+2)/2$ components. \mathbf{L}^k is a $n_l \times n_v$ matrix, with $n_l = (k+1)(k+2)$. This matrix involves the successive derivatives of the curvature of Γ at P . Computing \mathbf{L}^k with $k > 2$ is a tedious task, which can be greatly simplified by using computer algebra tools.

2.3 Compatibility conditions

The second spatial derivatives of stress components are linked together by the compatibility condition of Barré-de Saint Venant (Love, 1944)

$$\frac{\partial^2 \sigma_{xz}}{\partial x \partial z} = \alpha_2 \frac{\partial^2 \sigma_{xx}}{\partial x^2} + \alpha_1 \frac{\partial^2 \sigma_{zz}}{\partial x^2} + \alpha_1 \frac{\partial^2 \sigma_{xx}}{\partial z^2} + \alpha_2 \frac{\partial^2 \sigma_{zz}}{\partial z^2}, \quad (8)$$

with

$$\alpha_1 = \frac{\lambda + 2\mu}{4(\lambda + \mu)}, \quad \alpha_2 = -\frac{\lambda}{4(\lambda + \mu)}.$$

This compatibility condition is a necessary and sufficient condition for the strain tensor to be symmetrical. If $k \geq 2$, it can be differentiated $(k-2)$ -times in terms of x and z . With $k \geq 2$, one obtains $n_c = k(k-1)/2$ relations; with $k < 2$, $n_c = 0$. Unlike the boundary conditions, these compatibility conditions are satisfied everywhere in Ω : in particular, they are satisfied at P on Γ . The vector of boundary values \mathbf{U}^k can therefore be expressed in terms of a shorter vector $\hat{\mathbf{U}}^k$ with $n_v - n_c$ independent components

$$\mathbf{U}^k = \mathbf{G}^k \hat{\mathbf{U}}^k. \quad (9)$$

An algorithm for building the $n_v \times (n_v - n_c)$ matrix \mathbf{G}^k is given in Lombard & Piraux (2006).

3 THE DISCRETE PROBLEM

3.1 Numerical scheme

To integrate the hyperbolic system (1), we introduce a single Cartesian lattice of grid points: $(x_i, z_j, t_n) = (ih, jh, n\Delta t)$, where h is the mesh spacing and Δt is the time step. Unlike with staggered grids, all the unknowns are computed at the same grid nodes. The approximation $\mathbf{U}_{i,j}^n$ of $\mathbf{U}(x_i, z_j, t_n)$ is computed using any explicit, two-step, and spatially-centred finite-difference scheme. A review of the huge body of literature on finite-differences is given in LeVeque (1992) and Moczo et al. (2007).

Here we propose to use ADER schemes, that allow to reach easily arbitrary high-order of time and space accuracy (Schwartzkopff et al., 2005). On Cartesian grids, these finite-volume integration schemes originally developed for aeroacoustic applications are equivalent to finite-difference Lax-Wendroff-type integration schemes (Lörcher & Munz, 2005). In the numerical experiments described in section 4, we use a fourth-order ADER integration scheme. This scheme is stable under the Courant-Friedrichs-Lewy (CFL) condition $c_p \Delta t/h \leq 0.9$ in 2D; as usually with single-grid schemes, it is slightly dissipative (Schwartzkopff et al., 2005).

Many other single-grid schemes can be used in this context. In particular, the method described in the next subsections has been successfully combined with flux-limiter schemes (LeVeque, 1992) and with the standard second-order Lax-Wendroff scheme. Difficulties have been encountered with dissipative-free schemes based on centred staggered-grid finite-difference schemes, as we will see in section 3.6.

3.2 Use of fictitious values

Time-marching at grid-points where the stencil crosses Γ requires fictitious values of the solution in the vacuum, which have to be determined. The question arises as to how to compute, for instance, the fictitious value $\mathbf{U}_{I,J}^*$ at the grid point (x_I, z_J) in the vacuum, as sketched in Figure 2. Let $P(\tau)$ be the orthogonal projection of (x_I, z_J) on Γ , with coordinates $(x_P = x(\tau), z_P = z(\tau))$. At any grid point (x_i, z_j) , we denote

$$\mathbf{\Pi}_{i,j}^k = \left(\mathbf{I}_5, \dots, \frac{(x_i - x_P)^{\alpha-\beta} (z_j - z_P)^\beta}{(\alpha - \beta)! \beta!} \mathbf{I}_5, \dots, \frac{(z_j - z_P)^k}{k!} \mathbf{I}_5 \right)$$

the $5 \times n_v$ matrix containing the coefficients of k -th order Taylor expansions in space at P , where \mathbf{I}_5 is the 5×5 identity matrix, $\alpha = 0, \dots, k$, and $\beta = 0, \dots, \alpha$. The fictitious value $\mathbf{U}_{I,J}^*$ is defined as the Taylor-like extrapolation

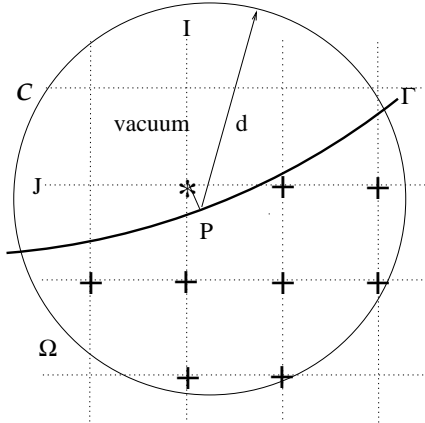


Figure 2. Determination of the fictitious value $U_{I,J}^*$ required for time-marching at neighboring grid nodes. P is the orthogonal projection of (x_I, z_J) on Γ . The n_p grid nodes in Ω and inside the circle \mathcal{C} centred at P with a radius d are denoted by \ast .

$$U_{I,J}^* = \Pi_{I,J}^k U^k, \quad (10)$$

where U^k defined by (7) still remains to be estimated.

3.3 Reduced vector of boundary values

Before determining U^k in (10), we first reduce the number of independent components it contains. The expressions obtained in section 2 are used for this purpose. The linear homogeneous system following from (6) and (9) is

$$L^k G^k \hat{U}^k = 0. \quad (11)$$

This system has fewer equations (n_l) than unknowns ($n_v - n_c$). It therefore has an infinite number of possible solutions that constitute a space with the dimension $n_v - n_c - n_l$. Let $K_{L^k G^k}$ be a $(n_v - n_c) \times (n_v - n_c - n_l)$ matrix containing the basis vectors of the kernel of $L^k G^k$. The general solution of (11) is therefore

$$\hat{U}^k = K_{L^k G^k} \bar{U}^k, \quad (12)$$

where the $n_v - n_c - n_l$ components of \bar{U}^k are real numbers. Injecting (12) into (9) gives

$$U^k = G^k K_{L^k G^k} \bar{U}^k. \quad (13)$$

The computation of $K_{L^k G^k}$ is a key point. For this purpose, we use a classical linear algebra tool: singular value decomposition of $L^k G^k$. Technical details can be found in the Appendix A of Lombard & Piraux (2004).

3.4 Computation of fictitious values

Let us now consider the n_p grid points of Ω in the circle \mathcal{C} centred at P with a radius d ; for instance, $n_p = 8$ in Figure 2. At these points, we write the k -th order Taylor expansion in space of the solution at P , and then we use the expression (13). This gives

$$\begin{aligned} U(x_i, z_j, t_n) &= \Pi_{i,j}^k U^k + O(h^{k+1}), \\ &= \Pi_{i,j}^k G^k K_{L^k G^k} \bar{U}^k + O(h^{k+1}). \end{aligned} \quad (14)$$

The set of n_p equations (14) is written compactly via a $5 n_p \times (n_v - n_c - n_l)$ matrix M

$$(U(\cdot, t_n))_{\mathcal{C}} = M \bar{U}^k + O(h^{k+1}), \quad (15)$$

where $(U(\cdot, t_n))_{\mathcal{C}}$ is the vector containing the exact values of the solution at the grid nodes of Ω inside \mathcal{C} . These exact values are replaced by the known numerical values $(U^n)_{\mathcal{C}}$, and Taylor rests are removed. From now on, numerical values and exact values of the fields are used indiscriminately. The discrete system thus obtained is overdetermined (see the remark (i) about d and typical values of n_p in subsection 3.5). We now compute its least-squares solution

$$\bar{U}^k = M^{-1} (U^n)_{\mathcal{C}}, \quad (16)$$

where the $(n_v - n_c - n_l) \times 5 n_p$ matrix M^{-1} denotes the pseudo-inverse of M . From (10), (13) and (16), the fictitious value in the vacuum at (x_I, z_J) is

$$\begin{aligned} U_{I,J}^* &= \Pi_{I,J}^k G^k K_{L^k G^k} M^{-1} (U^n)_{\mathcal{C}} \\ &= \Lambda_{I,J} (U^n)_{\mathcal{C}}. \end{aligned} \quad (17)$$

The $5 \times 5 n_p$ matrix $\Lambda_{I,J}$ is called the *extrapolator* at (x_I, z_J) . The fictitious values have no clear physical meaning. They only allow, by interpolation with numerical values inside Ω , to recover the high-order Dirichlet conditions (7).

3.5 Comments and practical details

The extrapolation method described in section 3.4 has to be applied at each grid point (I, J) in the vacuum where a fictitious value is required for the time-marching procedure. Useful comments are proposed about this method:

(i) The radius d of \mathcal{C} must ensure that the number of equations in (15) is greater than the number of unknowns:

$$\varepsilon(k, d) = \frac{5 n_p}{n_v - n_c - n_l} \geq 1. \quad (18)$$

No theoretical results are available about the optimal value of ε . However, numerical studies have shown that a definite overestimation ensures long-term stability: typically, $\varepsilon \approx 4$. Various strategies can be used to ensure (18), such as an adaptive choice of d depending on the local geometry of Γ at P . Here we adopt a simpler strategy consisting in using a constant radius d . With $k = 3$, numerical experiments have shown that $d = 3.2 h$ is a good candidate for this purpose. In this case, one typically obtains $n_p \approx 15$.

(ii) Since the boundary conditions do not vary with time, the extrapolators $\Lambda_{I,J}$ in (17) can be computed and stored during a pre-processing step. At each time step, only small matrix-vector products are required.

(iii) The extrapolators $\Lambda_{I,J}$ account for the local geometry of Γ at the projection points P on Γ via L^k (section 2.2). Moreover, they incorporate the position of P relative to the Cartesian meshing, via $\Pi_{i,j}$ (14) and $\Pi_{I,J}$ (17). The set of extrapolators therefore provides a subcell resolution of Γ in the meshing, avoiding the spurious diffractions induced by a naive description of the boundaries.

(iv) The stability of the method has not been proved. However, numerical experiments clearly indicate that the CFL condition of stability is not modified compared with the case of a homogeneous medium. The solution does not grow with time, even in the case of long-time simulations (see section 4.5).

(v) In a previous one-dimensional study (Piraux & Lombard, 2001), the local truncation error of the method has been rigorously analysed, leading to the following result: using the fictitious values (17) ensures a local r -th order spatial accuracy if $k \geq r$, where

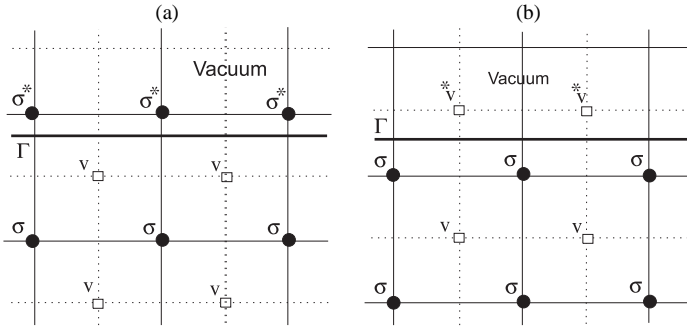


Figure 3. Staggered-grid schemes with a plane boundary Γ parallel to the meshing: two cases can be distinguished, depending on the position of Γ relative to the meshing. Case (a), where the fictitious stress is estimated, works well, while case (b), where the fictitious velocity is estimated, leads to long-term instabilities.

r is the order of spatial accuracy of the scheme. In 2D configurations with material interfaces (Lombard & Piraux, 2004, 2006), no proof has been conducted, but numerical experiments have shown that the r -th order overall accuracy is also maintained by taking $k = r$. Note that a slightly smaller order of extrapolation can be used: $k = r - 1$ suffices to provide r -th order overall accuracy (Gustafsson, 1975). The value $k = 3$ is therefore used for the fourth-order ADER scheme.

(vi) The extrapolators do not depend on the numerical scheme adopted. They depend only on k and on physical and geometrical features. Standard subroutines for computing the extrapolators $\Lambda_{I,J}$ can therefore be developed and adapted to a wide range of schemes. Subroutines of this kind are freely available in FORTRAN at the web page <http://w3lma.cnrs-mrs.fr/~MI/Software/>.

3.6 Case of staggered-grid schemes

Instead of using a single-grid scheme as proposed in section 3.1, readers may be interested in adapting our approach to staggered-grid schemes such as CSS or PSS (see section 1 for the definition of these terms). However, in the case of some of the boundary positions relative to the meshing, computational instabilities occur, especially when long-time integration is considered.

To understand why this is so, let us consider PSS-2. Taking a simple flat boundary to exist between the medium and the vacuum leads to two typical geometrical configurations. At one position of the free surface, the boundary discretization will require only the stress field to be extrapolated (Figure 3-(a)). Our procedure works satisfactorily with this type of discretization at any order k . It also yields stable and accurate solutions when dealing with PSS-4, contrary to the vacuum method. Using 10 grid nodes per minimal S-wavelength gives similar performance in this case to those of our numerical experiments based on the ADER scheme, which are shown in section 4.

At another position of the free surface where only extrapolated velocities are required within a wide zone (Figure 3-(b)), our procedure results in instabilities. The reason for this problem is as follows: fictitious velocities involve first-order boundary conditions (3) and higher-order conditions (see section 2.2), but they do not involve the fundamental zeroth-order Dirichlet conditions (2). Since the latter conditions are never enforced, an increasing oscillating drift occurs near the boundary, which invalidates the computations.

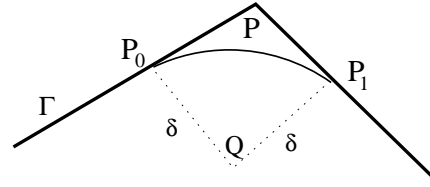


Figure 4. Boundary Γ with a corner at P , replaced locally by an arc of circle with a radius δ between P_0 and P_1 .

Similar behavior is observed with PSS-4, but after a longer time: the numerical solution generally works well during a few thousand time steps, before growing in a unstable manner.

The extrapolation method presented here is therefore not recommended for use with staggered-grid schemes, especially PSS-2, except in the trivial case sketched in Figure 3-(a).

3.7 Case of non-smooth geometries

Up to now, we have assumed that the boundary Γ was sufficiently smooth at the projection points, being at least C^{k+1} at each P , where $k \geq 0$ is the order of differentiation defined in section 3.5. Let us assume now that Γ is only C^K at a point P , with $K < k + 1$. Then, the components of \mathbf{L}^k in (6) involving the derivatives $\frac{d^\alpha x}{d\tau^\alpha}(\tau)$ and $\frac{d^\alpha z}{d\tau^\alpha}(\tau)$ ($\alpha = K + 1, \dots, k + 1$) of the parametric representation are discontinuous, invalidating locally the method proposed. In our software, we have implemented the following rough treatment:

- (i) If $K = 0$, the boundary owns a corner and the solution has an integrable singularity. The corner is replaced by an arc of circle centred at Q with radius δ (figure 4), leading to a C^1 curve.
- (ii) If $0 < K < k + 1$, as in the previous case at P_0 and P_1 with $K = 1$, the values of $\frac{d^\alpha x}{d\tau^\alpha}(\tau)$ and $\frac{d^\alpha z}{d\tau^\alpha}(\tau)$ ($\alpha = K + 1, \dots, k + 1$) are taken indiscriminately on one side or the other of the point considered.

No numerical instabilities were observed if δ (in case (i)) or the radius of curvature (in case (ii)) is much greater than h . It is agreed that the accuracy of computations is no more controlled in the cases (i) and (ii), especially the convergence towards the exact solution.

More sophisticated treatments of geometrical singularities, such as space-time mesh refinement (Berger & LeVeque, 1998), require further investigation, which is out of the scope of the present paper. New studies are also needed in the case of merging boundaries, occurring for instance when an internal material interface reaches the free surface (Moczo et al., 2004).

4 NUMERICAL EXPERIMENTS

4.1 Configurations

The time evolution of the source is a Ricker wavelet

$$g(t) = \{2(\pi f_c(t - t_c))^2 - 1\} e^{-\pi f_c(t - t_c)^2}, \quad (19)$$

where f_c is the central frequency, and $t_c = 1/f_c$. The maximal frequency f_{\max} defined by $|\tilde{g}(f_{\max})/\tilde{g}(f_c)| = 0.5$ (the tilde designates the Fourier transform) is $f_{\max} \approx 1.6 f_c$. We will adopt this frequency f_{\max} for our rule of thumb about the number of grid nodes per S-wavelength. The following values of the physical parameters will be used in all the following tests: $\rho = 2400 \text{ kg/m}^3$,

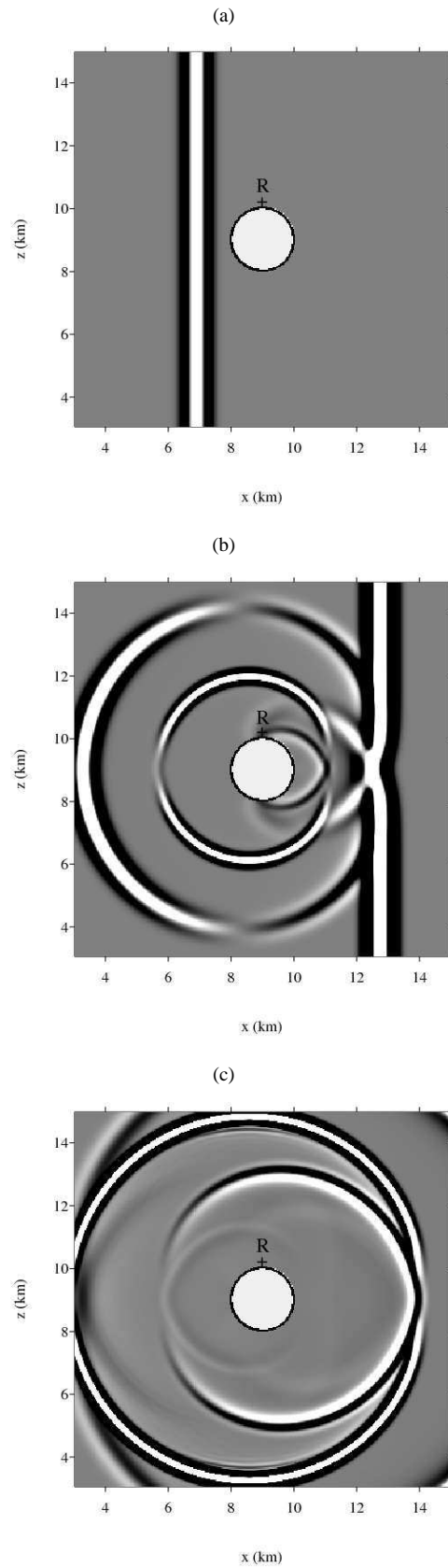


Figure 5. Test 1: snapshots of v_x at the initial instant (a), at mid-term (b) and at the final instant (c).

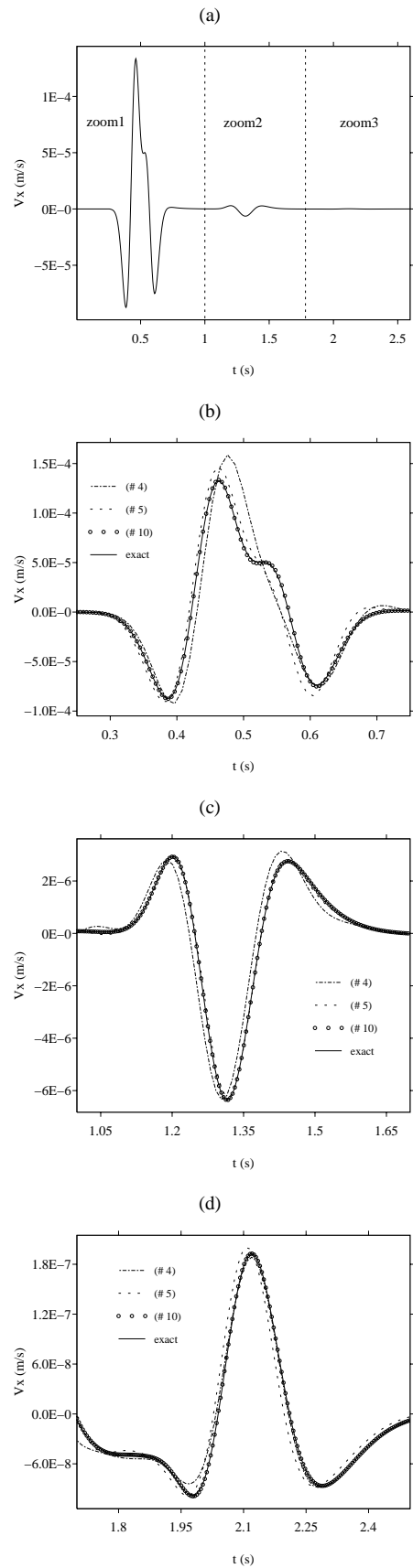


Figure 6. Test 1: time history of v_x (a). Zooms on successive time windows, with various discretizations (b,c,d): the number after # denotes the number of grid nodes per minimal S -wavelength.

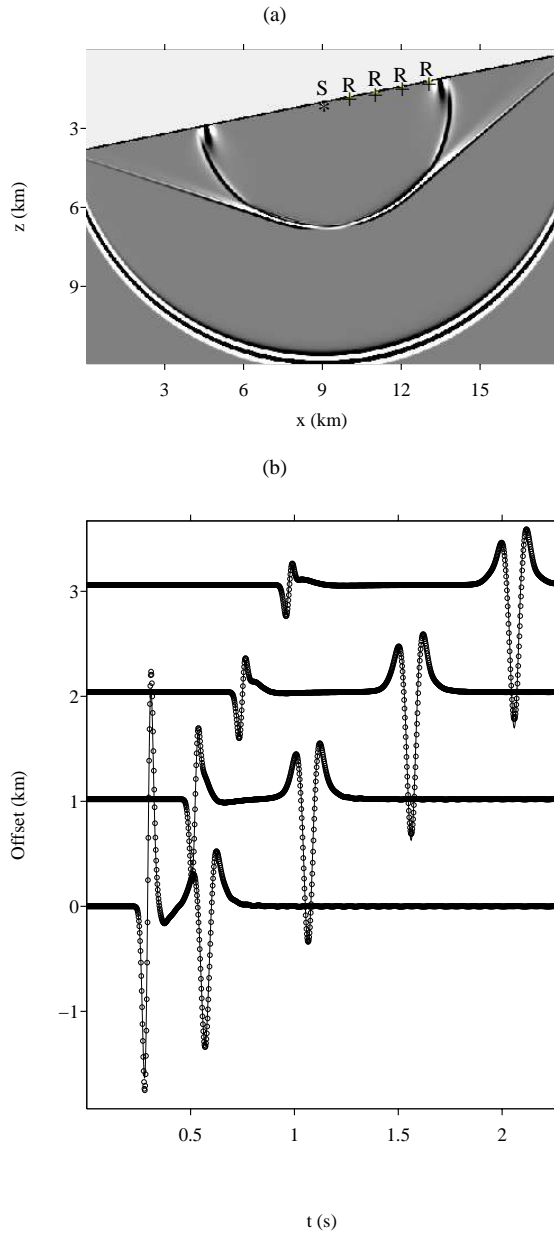


Figure 7. Test 2: snapshot of v_z at the final instant (a). Numerical and exact time histories of v_z (b).

$c_p = 4500$ m/s, and $c_s = 2200$ m/s. Lastly, the mesh size and the time step satisfy $c_p \Delta t/h = 0.85$.

The simulations are performed on a PC Pentium at 3 GHz with 2 GB of RAM. The results of tests 1 and 2, with constant and null curvature of Γ , compare quantitatively with analytical solutions denoted by a solid line. Test 3, with a variable curvature, is purely qualitative. Test 4 shows the slow decrease in the mechanical energy which occurs during very long integration times, which confirms the stability of the method.

4.2 Test 1: circular boundary

Computational efficiency. Let us consider a circular cavity containing vacuum, with radius 1 km, at the center of a $18 \text{ km} \times 18 \text{ km}$

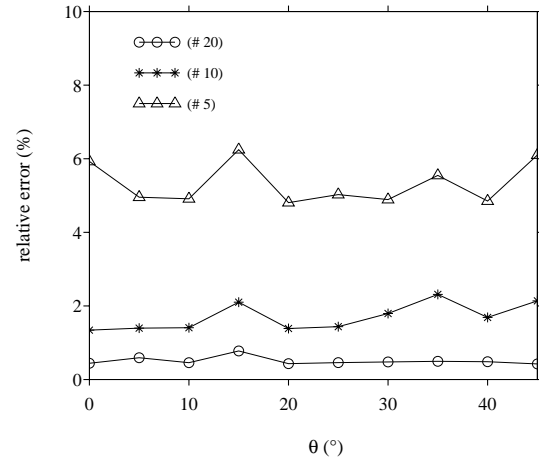


Figure 8. Test 2: parametric study of the relative error in terms of the boundary's angle θ , with various discretizations. The number after # denotes the number of grid nodes per minimal S-wavelength.

domain. In a first part, the mesh spacing is $h = 25$ m. The source is a rightward-moving plane wave, with $f_{\max} = 8$ Hz, ensuring 22 grid nodes per minimal P-wavelength and 10 grid nodes per minimal S-wavelength at that frequency.

During the pre-processing step, the program finds the 616 grid nodes where fictitious values are required; it also computes and stores the 616 extrapolators defined by the expression (17). Time integration is performed in 550 time steps, which corresponds to a propagation time of 2.75 s and a propagation distance of 22 minimal wavelengths. The preprocessing step takes 21 s of CPU time. The time integration takes 1100 s of CPU time, including 28.6 s induced by the computation and by the use of fictitious values, which amounts to an extra time cost of only 2.6 %. Figure 5 shows snapshots of v_x at the initial instant (a), after 275 time steps (b) and after 550 time steps (c).

Quantitative study. In a second part, three discretizations are considered: $h = 25$ m, 50 m, 60 m, corresponding respectively to 10, 5 and 4 grid nodes per minimal S-wavelength. A receiver is set just above the cavity, at the position (9 km, 10.2 km), that can be seen on Figure 5; it mainly records the waves propagating along the boundary. Numerically, these waves are highly sensitive to the quality of the fictitious values defined in section 3.

Figure 6-(a) shows the time history of v_x at the receiver. In this time window, three main wave packets are generated; with the scale of Figure 6-(a), the third packet cannot be seen. The amplitude is divided by a factor of approximately 30 from one packet to the following one. For the sake of clarity, zooms around each wave packet are shown in Figure 6-(b,c,d). These solutions are compared with an exact solution computed thanks to inverse Fourier transforms on 4096 frequencies, with $1.25 \cdot 10^{-2}$ Hz as the sampling frequency; each harmonic component is expanded into 60 Bessel modes. The agreement between the numerical and the analytical values is very good when 10 grid nodes per wavelength are used, even at very small amplitudes (d). For 5 and 4 grid nodes per wavelength, the solution is slightly less accurate, but it is still acceptable.

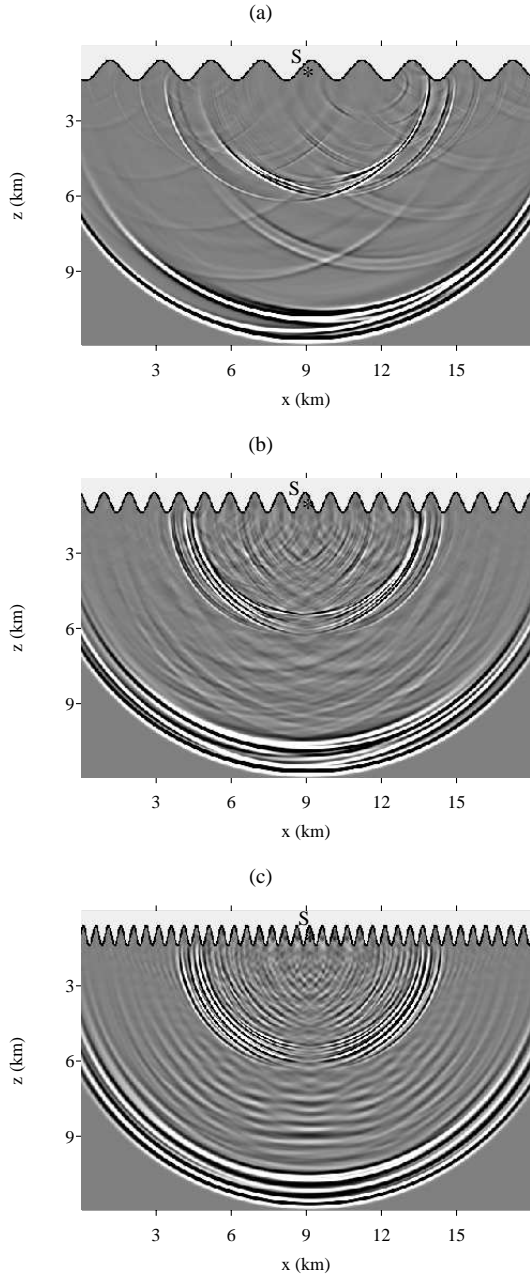


Figure 9. Test 3: snapshots of v_z , for various sinusoidal topographies.

4.3 Test 2: inclined straight boundary

The Garvin's problem. As a second test, we take a plane boundary inclined against the Cartesian mesh. The domain under investigation is 18 km wide and 12 km high, with the origin of the coordinates on the top and left. The mesh spacing is $h = 10$ m. Four receivers at (10 km, 1.8 km), (11 km, 1.6 km), (12 km, 1.4 km) and (13 km, 1.2 km) belong to the free boundary which is inclined at an angle of $\theta = 11.3^\circ$ relative to Ox .

An explosive source S is buried at (9 km, 2.1 km), with $f_{\max} = 24$ Hz. The distance between the source and the free surface is roughly $100 \text{ m} < \lambda_p/3$, where λ_p is the wavelength of the compressional waves at frequency f_c , and hence large Rayleigh waves are generated, with a velocity $c_r = 2054$ m/s. To prevent

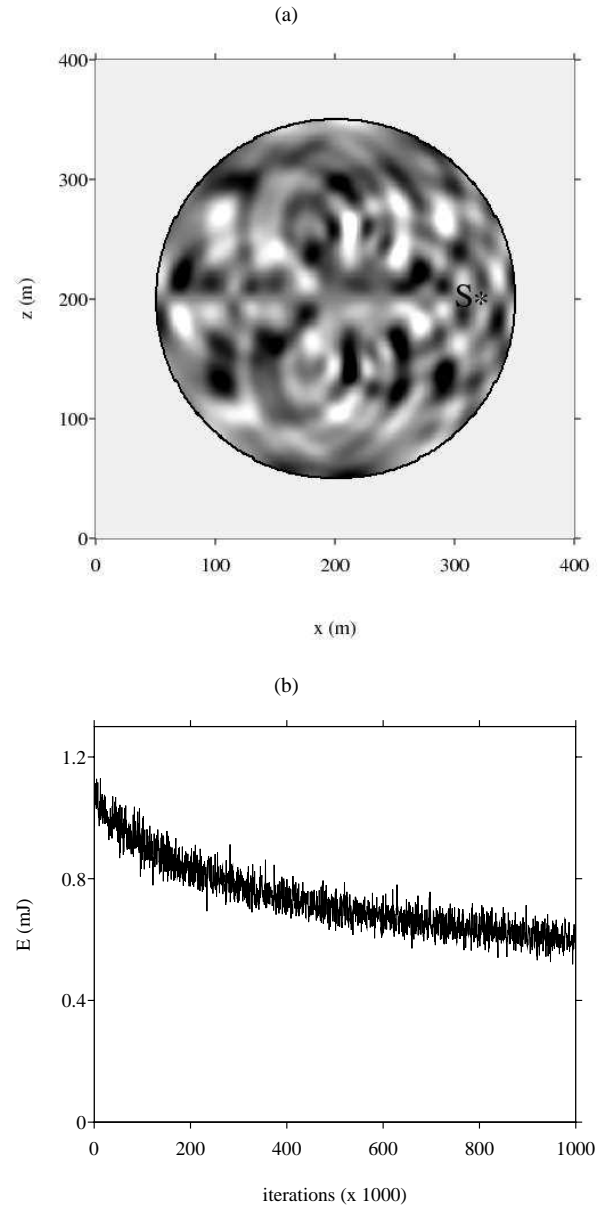


Figure 10. Test 4: snapshot of v_z (a) and time history of the mechanical energy (b).

the occurrence of spurious oscillations, the source is spread out numerically over a radius of $R = \lambda_p/7.5 = 40$ m. The source is weighted by a gaussian law with a standard deviation $R/2 = 20$ m. The spatial discretization ensures the sampling of roughly 18 grid nodes per minimal P-wavelength, and 9 grid nodes per minimal S-wavelength at the frequency f_{\max} .

Figure 7-(a) shows a snapshot of v_z after 1200 time steps, corresponding to a propagation time of 2.25 s and a propagation distance of 55 minimal wavelengths. Direct cylindrical waves are observed, together with converted PP waves, converted PS waves (with an almost linear wavefront), and Rayleigh waves. In Figure 7-(b), the time history of v_z recorded at the receivers can be favourably compared with an exact solution. The latter is obtained by convolving the Green's function obtained by the well-known Cagniard-de Hoop method (Garvin, 1955;

Sánchez-Sesma & Iturrarán-Viveros, 2006) with the source wavelet (19) and with the discrete source spreading.

Influence of the slope. To quantify the effects of the angle between the boundary and the Cartesian meshing on the numerical solution, we perform a parametric study of the error in terms of θ . Ten angles are considered, from $\theta = 0^\circ$ to $\theta = 45^\circ$ in steps of 5° . In each configuration, the waves are measured at the free boundary after propagating for 65 minimal wavelengths. The error of $v \cdot n$ is measured in norm L_2 , and then it is normalized by the norm L_2 of the exact time history of $v \cdot n$.

The results of this study are shown in Figure 8, with various discretizations: 5, 10, 20 grid nodes per minimal S-wavelength. With a given h , the error is almost constant and independent of θ . This constitutes a crucial advantage of our method over the vacuum method, where the error at 45° is much greater than that at 0° : it means that an extremely fine discretization is required to obtain accurate results with the vacuum method when arbitrary-shaped boundaries are encountered (Bohlen & Saenger, 2006).

4.4 Test 3: sinusoidal boundary

Since boundaries not related to the finite-difference grid can be included, the third test is performed on a sinusoidal free boundary, with a peak-to-peak amplitude of 800 m and various wavelengths: 0.5 km, 1 km and 2 km. The sinusoidal curve is centred around $z = 1$ km. The source S is located at (9 km, 1 km). The other parameters are the same as in test 2. Figure 9 shows snapshots of v_z at the final instant 2.25 s. One can clearly see how the wavelength of the sinusoidal boundary influences the diffracted fields.

Convergence studies (not shown here) were performed in these three cases, by comparing solutions computed on finer grids. We again concluded that accurate solutions can be obtained when the simulations involve approximately 10 grid nodes per minimal S-wavelength at the frequency f_{\max} of the source wavelet, even in the case of complex topographies with variable curvatures.

4.5 Test 4: long-term stability

The fourth test focuses on long-term stability (Stacey, 1994; Hestholm, 2003). For this purpose, we consider a circular elastic domain with a radius of 150 m, surrounded by vacuum. The source S is located inside the circle, at (320 m, 200 m). This configuration is obviously not realistic, but it enlightens the influence of the boundary on the numerical solution after many reflections, and especially on the possible excitation of numerical spurious modes leading to long-term instability. The mesh size is $h = 1$ m. Time integration is performed during 10^6 time steps, with $f_{\max} = 160$ Hz.

Figure 10-(a) shows a snapshot of v_z at the final instant: no instability is observed, and the antisymmetry of v_z is satisfied. Once the source is extincted ($t > 2t_c$), the mechanical energy E is theoretically maintained. It can be written in terms of v and σ

$$E = \frac{1}{2} \int_{\Omega} \int_{\Omega} \left\{ \rho v^2 + \frac{\lambda + 2\mu}{4\mu(\lambda + \mu)} (\sigma_{xx}^2 + \sigma_{zz}^2) + \frac{1}{\mu} \sigma_{xz}^2 - \frac{\lambda}{2\mu(\lambda + \mu)} \sigma_{xx} \sigma_{zz} \right\} dx dz. \quad (20)$$

At each time step, the integral in (20) is estimated by a basic trapezoidal rule at the grid nodes inside Ω . Figure 10-(b) shows the time history of this mechanical energy so-obtained. It slightly decreases, due to the numerical diffusion of the scheme, which confirms that the method is stable.

5 CONCLUSION

Here we have presented a method of incorporating free boundaries into time-domain single-grid finite-difference schemes for elastic wave simulations. This method is based on fictitious values of the solution in the vacuum, which are used by the numerical integration scheme near boundaries. These high-order fictitious values accurately describe both the boundary conditions and the geometrical features of the boundaries. The method is robust, involving negligible extra computational costs.

Unlike the vacuum method, the quality of the numerical solution thus obtained is almost independent of the angle between the free boundaries and the Cartesian meshing. Since the free boundaries do not introduce any additional artefacts, one can use the same discretization as in homogeneous media. Typically, when a fourth-order ADER scheme is used on a propagation distance of 50 minimal wavelengths, 10 grid nodes per minimal S-wavelength yield to a very good level of accuracy. With 5 grid nodes per minimal S-wavelength, the solution is less accurate but still acceptable.

For the sake of simplicity, we have dealt here with academic cases, considering two-dimensional geometries, constant physical parameters, and simple elastic media. Let us examine briefly the generalization of our approach to more realistic configurations:

(i) Extending the method to 3-D topographies a priori does not require new tools. The main challenge will concern the computational efficiency of parallelization. A key point is that the determination of each fictitious value is local, using numerical values only at neighboring grid nodes. Particular care will however be required for fictitious values near frontiers between computational subdomains, in order to minimize the exchanges of data.

(ii) Near free boundaries, the domains of propagation are usually smoothly heterogeneous. To generalize our method to continuously variable media, the main novelty expected concerns the high-order boundary conditions detailed in section 2.2. With variable matrices \mathbf{A} and \mathbf{B} indeed and $k \geq 2$, the procedure (5) will involve the following quantities, to be estimated numerically:

$$\frac{\partial^{k-1}}{\partial x^{k-1-\alpha} \partial z^\alpha} \mathbf{A}, \quad \frac{\partial^{k-1}}{\partial x^{k-1-\alpha} \partial z^\alpha} \mathbf{B}, \quad \alpha = 0, \dots, k-1.$$

(iii) Realistic modeling of wave propagation requires to incorporate attenuation. The only rheological viscoelastic models able to approximate constant quality factor over a frequency range are the generalized Maxwell body (Emmerich & Korn, 1984) and the generalized Zener body (Carcione, 2001). These two equivalent models (Moczo & Kristek, 2005) yield to additional unknowns called *memory variables*. In the time domain, the whole set of unknowns satisfies a linear hyperbolic system with source term

$$\frac{\partial}{\partial t} \mathbf{U} = \mathbf{A} \frac{\partial}{\partial x} \mathbf{U} + \mathbf{B} \frac{\partial}{\partial z} \mathbf{U} - \mathbf{S} \mathbf{U}, \quad (21)$$

where \mathbf{S} is a definite positive matrix. Compared with the elastic case (1) examined in the present paper, the main difference expected concerns the time differentiation of the boundary condition (2). Indeed, equation (3) has to be modified accordingly to (21). Similar modifications are also foreseen in the case of poroelasticity in the low-frequency range (Dai et al., 1995), where the evolution equations can be put in the form (21).

ACKNOWLEDGMENTS

The authors thank the reviewers P. Moczo and I. Oprsal for their instructive comments and bibliographic insights.

References

- Ben Jemaa, M., Glinsky-Olivier, N., Virieux, V. M. C.-A. J., & Piperno, S., 2007. Dynamic non-planar crack rupture by a finite-volume method, *Geophys. J. Int.*, **accepted**.
- Berger, M. J. & LeVeque, R. J., 1998. Adaptive mesh refinement using wave-propagation algorithms for hyperbolic systems, *SIAM J. Numer. Anal.*, **35**, 2298–2316.
- Bohlen, T. & Saenger, E., 2003. 3-D viscoelastic finite-difference modeling using the rotated staggered grid: tests of accuracy, *65th Annual International Meeting, EAGE, Extended Abstracts*, **C44**.
- Bohlen, T. & Saenger, E., 2006. Accuracy of heterogeneous staggered-grid finite-difference modeling of Rayleigh waves, *Geophysics*, **71**, T109–T115.
- Carcione, J. M., 2001. *Wave Fields in Real Media: Wave Propagation in Anisotropic, Anelastic and Porous Media*, Pergamon, New York.
- Carpenter, M., Gottlieb, D., & Arbanell, S., 1994. Time-stable boundary conditions for finite-difference schemes solving hyperbolic schemes: methodology and application to high-order compact schemes, *J. Comput. Phys.*, **111**, 220–236.
- Cruz-Atienza, V. & Virieux, J., 2004. Dynamic rupture simulation of non-planar faults with a finite-difference approach, *Geophys. J. Int.*, **158**, 939–954.
- Dai, N., Vafidis, A., & Kanasevich, E., 1995. Wave propagation in heterogeneous porous media: a velocity-stress, finite-difference method, *Geophysics*, **60**, 327–340.
- Day, S., 1977. *Finite element analysis of seismic scattering problems*, Ph.D. thesis, University of San-Diego.
- Dumbser, M. & Käser, M., 2006. An arbitrary high-order discontinuous Galerkin method for elastic waves on unstructured meshes - II. The three-dimensional isotropic case, *Geophys. J. Int.*, **167**, 319–336.
- Emmerich, H. & Korn, M., 1984. Incorporation of attenuation into time-domain computations of seismic wave fields, *Geophysics*, **52**, 1252–1264.
- Garvin, W., 1955. Exact transient solution of the buried line source problem, *Proc. R. Soc. London Ser. A*, **234**, 528–541.
- Gélis, C., Leparoux, D., Virieux, J., Bitri, A., Operto, S., & Grandjean, G., 2005. Numerical modeling of surface waves over shallow cavities, *J. Environ. Engin. Geophys.*, **10**, 49–59.
- Graves, R., 1996. Simulating seismic wave propagation in 3-D elastic media using staggered-grid finite differences, *Bull. Seismo. Soc. Am.*, **86**, 1091–1106.
- Gustafsson, B., 1975. The convergence rate for difference approximations to mixed initial boundary value problems, *Math. Comp.*, **29**, 396–406.
- Hestholm, S., 2003. Elastic wave modeling with free surfaces: stability of long simulations, *Geophysics*, **68**, 314–321.
- Jih, R., McLaughlin, K., & Der, Z., 1988. Free-boundary conditions of arbitrary polygonal topography in a two-dimensional explicit finite-difference scheme, *Geophysics*, **53**, 1045–1055.
- Kelly, K., Ward, R., Treitel, S., & Alford, R., 1976. Synthetic seismograms: a finite-difference approach, *Geophysics*, **41**, 2–27.
- Komatitsch, D. & Vilotte, J., 1998. The spectral element method: an efficient tool to simulate the seismic response of 2-D and 3-D geological structures, *Bull. Seismo. Soc. Am.*, **88**, 368–392.
- Levander, A., 1988. Fourth-order finite-difference p-sv seismograms, *Geophysics*, **53**, 1425–1436.
- LeVeque, R., 1992. *Numerical Methods for Conservation Laws*, Birkhäuser, Basel, Switzerland.
- Lombard, B. & Piraux, J., 2004. Numerical treatment of two-dimensional interfaces for acoustic and elastic waves, *J. Comput. Phys.*, **195**, 90–116.
- Lombard, B. & Piraux, J., 2006. Numerical modeling of elastic waves across imperfect contacts, *SIAM J. Sci. Comput.*, **28**, 172–205.
- Lörcher, F. & Munz, C., 2005. Lax-Wendroff-type schemes of arbitrary order in several space dimensions, *IMA J. Num. Anal.*, pp. 1–28.
- Love, A., 1944. *A Treatise on the Mathematical Theory of Elasticity*, Dover Publications, New York, USA.
- Moczo, P. & Kristek, J., 2005. On the rheological models used for time-domain methods of seismic wave propagation, *Geophys. Res. Lett.*, **32**, L01306, doi: 1029/2004GL021598.
- Moczo, P., Kristek, J., Vavrycuk, J., Archuleta, R., & Halada, L., 2002. 3-D heterogeneous staggered-grid finite-difference modeling of seismic motion with volume harmonic and arithmetic averaging of elastic moduli and densities, *Bull. Seismo. Soc. Am.*, **92**, 3042–3066.
- Moczo, P., Kristek, J., & Galis, M., 2004. Simulation of the planar free surface with near-surface lateral discontinuities in the finite-difference modeling of seismic motion, *Bull. Seismo. Soc. Am.*, **94**, 760–768.
- Moczo, P., Robertsson, J. O., & Eisner, L., 2007. *The Finite-Difference Time-Domain Method for Modeling of Seismic Wave Propagation*. In *Advances in Wave Propagation in Heterogeneous Earth*, vol. 48, Elsevier Academic Press.
- Muir, F., Dellinger, J., Etgen, J., & Nichols, D., 1992. Modeling elastic fields across irregular boundaries, *Geophysics*, **57**, 1189–1193.
- Piroux, J. & Lombard, B., 2001. A new interface method for hyperbolic problems with discontinuous coefficients: one-dimensional acoustic example, *J. Comput. Phys.*, **168**, 227–248.
- Robertsson, J., 1996. A numerical free-surface condition for elastic / viscoelastic finite-difference modeling in the presence of topography, *Geophysics*, **61**, 1921–1934.
- Rodrigues, D., 1995. *Large Scale Modelling of Seismic Wave Propagation*, PhD Thesis, Ecole Centrale Paris.
- Saenger, E. & Bohlen, T., 2004. Finite-difference modeling of viscoelastic and anisotropic wave propagation using the rotated staggered grid, *Geophysics*, **69**, 583–591.
- Saenger, E. H., Gold, N., & Shapiro, S. A., 2000. Modeling the propagation of elastic waves using a modified finite-difference grid, *Wave Motion*, **31**, 77–92.
- Sánchez-Sesma, F. & Iturrarán-Viveros, U., 2006. The classical Garvin’s problem revisited, *Bull. Seismo. Soc. Am.*, **96**, 1344–1351.
- Schwartzkopff, T., Dumbser, M., & Käser, M., 2005. Fast high order finite volume schemes for linear wave propagation, *Numerische Mathematik*.
- Stacey, R., 1994. New finite-difference methods for free surfaces with a stability analysis, *Bull. Seismo. Soc. Am.*, **84**, 171–184.
- Tessmer, E. & Kosloff, D., 1994. 3-D elastic modeling with surface topography by a Chebyshev spectral method, *Geophysics*, **59**, 464–473.
- Virieux, J., 1986. P-SV wave propagation in heterogeneous media: velocity-stress finite-difference method, *Geophysics*, **51**, 889–901.
- Zahradník, J., 1995. Simple elastic finite-difference scheme, *Bull. Seismo. Soc. Am.*, **85**, 1879–1887.
- Zhang, W. & Chen, X., 2006. Traction image method for irregular free surface boundaries in finite-difference seismic wave simulation, *Geophys. J. Int.*, **167**, 337–353.